

---

---

# Small-Animal PET of Tumor Angiogenesis Using a $^{76}\text{Br}$ -Labeled Human Recombinant Antibody Fragment to the ED-B Domain of Fibronectin

Raffaella Rossin<sup>1</sup>, Dietmar Berndorff<sup>2</sup>, Matthias Friebe<sup>2</sup>, Ludger M. Dinkelborg<sup>2</sup>, and Michael J. Welch<sup>1</sup>

<sup>1</sup>Mallinckrodt Institute of Radiology, Washington University School of Medicine, St. Louis, Missouri; and <sup>2</sup>Bayer Schering Pharma, Global Drug Discovery, Berlin, Germany

---

The aim of this study was to image the extra domain B (ED-B) of fibronectin, an angiogenesis-related target, in solid tumors using small-animal PET. Toward this aim, an ED-B fibronectin-binding human antibody derivative (L19-SIP) was labeled with  $^{76}\text{Br}$  via an enzymatic approach. Biodistribution and imaging studies were performed in human teratoma-bearing mice for up to 48 h after injection. **Methods:** L19-SIP was labeled with  $^{76}\text{Br}$  using bromoperoxidase/ $\text{H}_2\text{O}_2$ . The stability of the labeled antibody was tested both in vitro and in vivo. Biodistribution and small-animal imaging studies (PET and CT) were performed in F9-bearing 129/sv mice ( $n = 3$  or 4). **Results:** The enzymatic radiobromination approach afforded the labeled antibody in high yield (>55%) under mild reaction conditions.  $^{76}\text{Br}$ -L19-SIP stability in mouse serum proved to be similar to that of the  $^{125}\text{I}$ -labeled analog (>80% of intact material at 48 h after injection). Fast and specific in vivo targeting was obtained in tumors and other organs expressing ED-B fibronectin (i.e., ovaries and uterus). However, slow renal clearance and persistent activity predominately in blood and stomach suggests partial  $^{76}\text{Br}$ -L19-SIP debromination in vivo. This debromination was confirmed in a metabolism study in normal mice. The F9 tumors were clearly imaged by small-animal PET at each considered time point, starting at 5 h up to 48 h after injection. **Conclusion:**  $^{76}\text{Br}$ -L19-SIP specifically accumulated at the target site, enabling detailed small-animal PET of tumor neovasculature. Therefore, targeting the angiogenesis-associated expression of ED-B fibronectin can be a valuable tool for tumor detection using molecular imaging with PET.

**Key Words:** angiogenesis; ED-B; fibronectin; L19-SIP;  $^{76}\text{Br}$ ; PET

**J Nucl Med 2007; 48:1172–1179**

DOI: 10.2967/jnumed.107.040477

---

**A** key parameter for tumorigenesis and rapid tumor growth is a strong vascularization. Access to the host vascular system and the generation of new blood vessels are, therefore, rate-determining steps in tumor growth. Small,

dormant tumors (1–2 mm) rely on oxygen and nutrient diffusion from the surrounding tissues to survive (avascular phase). Tumor progression and metastasis propagation occur only after induction of a tumor vasculature (angiogenic switch) (1). Therefore, angiogenic activity is an interesting target for a specific personalized tumor therapy. Currently, many new potential antiangiogenic agents are under evaluation in clinical trials. A reliable patient selection as well as an early therapy-monitoring tool will be a prerequisite for an efficient therapy development and patient management (2). The first PET studies in prostate cancer patients undergoing antiangiogenic therapy have been performed by monitoring changes in tumor blood flow ( $^{15}\text{O}$ -water), blood volume ( $^{11}\text{CO}$ ), and tumor metabolism ( $^{18}\text{F}$ -FDG) (3).  $^{11}\text{C}$ -Methionine uptake has also been suggested as a surrogate marker for an indirect measure of tumor angiogenesis (4). However, more direct visualization of tumor vasculature and better evaluation of changes after antiangiogenic therapy can be obtained by targeting specific proteins involved in the angiogenic process. Among these, the vascular endothelial growth factor receptor (VEGFR) (5–7) and the  $\alpha_v\beta_3$  integrin have been extensively evaluated for PET of angiogenesis (8–14).

The fibronectin splice variant B (ED-B) is another specific biomarker of angiogenesis (15). In fact, it is expressed around the neovasculature of a variety of human cancers, both in primary and metastatic sites (16,17) as well as in fetal tissues and in the female reproductive system, where tissue remodeling and angiogenesis are ongoing or recurrent processes. Therefore, imaging the expression of ED-B fibronectin may be a very useful tool to assess the efficacy of antiangiogenic therapies at an early stage.

Recently, a human recombinant scFv fragment (L19) has been developed with subnanomolar binding affinity for ED-B of fibronectin (18). In a preliminary clinical study, liver metastases of colon carcinoma, small cell lung cancer, and recurrent glioblastoma were imaged using an  $^{123}\text{I}$ -labeled L19(scFv)<sub>2</sub> (19). After that, several L19 formats were developed and evaluated in vivo for both radioimmunotherapy (20–23) and imaging (24). Among these, the L19 small immunoprotein (SIP) demonstrated the best performance in

---

Received Feb. 2, 2007; revision accepted Apr. 17, 2007.

For correspondence or reprints contact: Michael J. Welch, PhD, Mallinckrodt Institute of Radiology, Washington University School of Medicine, 510 S. Kingshighway Blvd., Campus Box 8225, St. Louis, MO 63110.

E-mail: welchm@wustl.edu

COPYRIGHT © 2007 by the Society of Nuclear Medicine, Inc.

vivo in terms of tumor targeting and clearance from non-target organs (20,25).

Driven by these promising results, we decided to explore the use of L19-SIP for PET of tumor neovasculature as this could be a particularly attractive imaging approach, providing both high spatial-resolution images and quantitative information on tracer distribution. Because of the biologic half-life of L19-SIP, a positron-emitting radionuclide with a half-life longer than that of  $^{18}\text{F}$  (109 min) was needed for PET of ED-B fibronectin. Among the radiohalogens, the positron emitters  $^{76}\text{Br}$  (half-life [ $t_{1/2}$ ] = 16.2 h) and  $^{124}\text{I}$  ( $t_{1/2}$  = 4.18 d) are under investigation for the production of PET radiotracers. There is considerable interest in  $^{76}\text{Br}$  labeling of antibodies (26–31) because of its favorable half-life that allows imaging up to 48 h after injection, its high production yields (at least an order of magnitude higher than that of  $^{124}\text{I}$ ), and its 54% positron emission (~2-fold higher than that of  $^{124}\text{I}$ ) (32). For these reasons, and due to the well-established labeling chemistry, we have labeled L19-SIP with  $^{76}\text{Br}$ . Small-animal PET and biodistribution studies were performed to evaluate the potential of such a PET probe. The results clearly indicated ED-B fibronectin targeting in vivo, thus confirming the possible use of L19-SIP to image angiogenesis with PET.

## MATERIALS AND METHODS

### Reagents

Unless otherwise listed, all solvents and reagents were purchased from Sigma-Aldrich and used as received. NAP-5 columns were purchased from GE Healthcare Biosciences. Water was distilled and then deionized (18 M $\Omega$ /cm $^2$ ) by passing through a Milli-Q water filtration system (Millipore Corp.). L19-SIP was expressed and purified as described earlier (25).  $^{76}\text{Br}$  was produced at the Washington University cyclotron facility by the  $^{76}\text{Se}(p,n)^{76}\text{Br}$  nuclear reaction on a  $^{76}\text{Se}$ -enriched  $\text{Cu}_2\text{Se}$  target.  $^{76}\text{Br}$  was recovered via a dry distillation method modified from that of Tolmachev et al. (33). The radionuclide solution (in 0.6 mol/L  $\text{NH}_4\text{OH}$ ) was filtered through a C-18 Sep-Pak light cartridge (Waters Corp.) and blown down to dryness. The radioactive bromide was reconstituted in the radiolabeling buffer shortly before use.  $^{125}\text{I}$ -Iodide was purchased from GE Healthcare Biosciences. Fast-protein liquid chromatography (FPLC) and radio-FPLC were performed using an Amersham Pharmacia Biotech ÄKTA FPLC system (GE Healthcare Biosciences) equipped with a model 170 Radioisotope Detector (Beckman Instruments). FPLC analysis was performed by injecting a 2- $\mu\text{L}$  analyte aliquot into a Superose 12 gel filtration column (GE Healthcare Biosciences), which was eluted with 20 mmol/L *N*-(2-hydroxyethyl)piperazine-*N'*-(2-ethanesulfonic acid) (HEPES) and 150 mmol/L NaCl buffer (pH 7.3) at an isocratic flow rate of 0.8 mL/min. The ultraviolet wavelength was preset at 280 nm. Under these conditions, the retention times of ( $^{76}\text{Br}$ )L19-SIP and  $^{76}\text{Br}$ -bromide were 16.9–17.1 min and 27.8 min, respectively.

### L19-SIP Radiolabeling

The  $^{76}\text{Br}$ -bromination protocol was modified from that of Lovqvist et al. (28). One hundred micrograms of L19-SIP were mixed with ~25–90 MBq (~0.67–2.43 mCi)  $^{76}\text{Br}$  and 0.6 unit

bromoperoxidase (BPO) in 300  $\mu\text{L}$  50 mmol/L phosphate buffer (pH 7.0) containing 80  $\mu\text{mol/L}$   $\text{H}_2\text{O}_2$ . The reaction mixture was incubated at 0°C and monitored by radio-FPLC. The radiobrominated antibody was purified by chromatography using a NAP-5 column eluted with 0.8 mL phosphate-buffered saline (PBS) and then analyzed by radio-FPLC. Samples having >90% radiochemical purity (RCP) were further diluted with PBS and used for animal studies. The immunoreactivity of  $^{76}\text{Br}$ -L19-SIP was determined by affinity chromatography as previously reported (20,24). The radioiodination ( $^{125}\text{I}$ ) of L19-SIP was performed as previously reported (20,24). The in vitro stability of the  $^{76}\text{Br}$ -L19-SIP and  $^{125}\text{I}$ -L19-SIP was evaluated by incubating duplicate samples of the compound in mouse serum (Sigma-Aldrich) at 37°C and by analyzing aliquots (filtered through 0.45  $\mu\text{m}$ ) by radio-FPLC at different time points up to 48 h.

### Cell Lines and Animals

Mouse embryonal teratocarcinoma cells (F9), obtained from American Type Culture Collection, were cultivated in Dulbecco's modified Eagle medium with Glutamax (Invitrogen Corp.) supplemented with 10% (v/v) fetal calf serum and maintained at 37°C in a humidified atmosphere containing 5%  $\text{CO}_2$ . Four-week-old female 129/sv mice (Charles River Laboratories) were injected with  $1 \times 10^6$  F9 cells in 100  $\mu\text{L}$  PBS subcutaneously into the right hindlimb. After 11 d, the animals were used for biodistribution and imaging experiments (tumor weight, 0.1–2.8 g). All animal studies were performed in compliance with guidelines set by the Washington University Animal Studies Committee.

### Biodistribution Studies

The F9 tumor-bearing mice ( $n = 3$  or 4 per time point) were anesthetized with isoflurane and injected intravenously with ~1.3 MBq of  $^{76}\text{Br}$ -L19-SIP (~185 kBq/ $\mu\text{g}$ ) in 150  $\mu\text{L}$  via the femoral vein. At 5, 24, and 48 h after injection, the mice were anesthetized and sacrificed by cervical dislocation. Organs and tissues of interest were removed, blotted dry, weighed, and counted. Diluted standard doses (1:100) were prepared and counted along with the samples to calculate the percentage injected dose per gram (%ID/g) and the percentage injected dose per organ (%ID/organ). All data were corrected for radioactive decay of  $^{76}\text{Br}$ .

### Small-Animal PET Studies

F9 tumor-bearing mice ( $n = 4$ ) were anesthetized with isoflurane and injected intravenously with ~13 MBq of  $^{76}\text{Br}$ -L19-SIP (~440 kBq/ $\mu\text{g}$ ) in 150  $\mu\text{L}$  via the femoral vein. The imaging sessions were performed at 5 h (one 15-min frame), 24 h, and 48 h after injection (one 30-min frame) using the microPET Focus (Siemens Medical Solutions USA, Inc.). At 24 and 48 h after injection, the mice underwent also microCT imaging (MicroCAT II; CTI-Imtek). microPET images (corrected for attenuation, scatter, normalization, and camera dead-time) and microCT images were coregistered using a landmark registration technique (by using fiducial markers directly attached to the animal bed) and AMIRA image display software (AMIRA; TGS Inc.). Data analysis of microPET images was performed using the manufacturer's software (ASIPRO; Siemens Medical Solutions). Data were calculated in terms of the standardized uptake values (SUVs) in 3-dimensional (3D) regions of interest (ROIs) using the following equation:

$$\text{SUV} = \frac{\text{Radioactivity concentration in ROI } [\mu\text{Ci}/\text{mL}]}{\text{Injected dose } [\mu\text{Ci}] / \text{Animal weight } [\text{g}]}$$

### In Vivo Metabolism Studies

Normal female BALB/c mice ( $n = 3$  per time point) weighing  $\sim 20$  g were anesthetized with isoflurane and injected intravenously with  $\sim 1.8$  MBq of  $^{76}\text{Br}$ -L19-SIP ( $\sim 185$  kBq/ $\mu\text{g}$ ) in 150  $\mu\text{L}$  via the tail vein. The mice were anesthetized before sacrifice at each time point (2, 5, and 24 h after injection). Blood and urine samples were collected. Serum ( $\sim 150$   $\mu\text{L}$ ) was separated from blood in Microtainer tubes (Becton, Dickinson and Co.). The residual immunoreactivity in serum was determined; then serum and urine samples were filtered through 0.45  $\mu\text{m}$  and analyzed by radio-FPLC.

## RESULTS

### L19-SIP Radiolabeling with $^{76}\text{Br}$

L19-SIP was reacted with different amounts of  $^{76}\text{Br}$  ( $\sim 25$  MBq ( $\sim 0.67$  mCi) or  $\sim 90$  MBq ( $\sim 2.43$  mCi) per 100  $\mu\text{g}$  antibody) for biodistribution and imaging studies. When reacting the compound with low amounts of  $^{76}\text{Br}$  ( $< 37$  MBq),  $82\% \pm 2\%$  radiolabeling yield was achieved in 80 min ( $n = 4$ ) (Fig. 1). When using higher amounts of  $^{76}\text{Br}$  ( $> 37$  MBq), the  $^{76}\text{Br}$  solution recovered from the target processing was blown down to dryness and then reconstituted in the labeling buffer immediately before the reaction to avoid radiolytic effects. Under these conditions, 55% radiochemical yield was achieved in 80 min ( $n = 2$ ). A complete separation between the radiolabeled product and the residual free  $^{76}\text{Br}$ -bromide could not be achieved with the NAP-5 chromatographic method. However, the  $^{76}\text{Br}$ -L19-SIP used for animal experiments had  $> 90\%$  RCP, as confirmed by radio-FPLC (Fig. 2B). The immunoreactivity of  $^{76}\text{Br}$ -L19-SIP was  $80\% \pm 2\%$  ( $n = 5$ ), as measured by affinity chromatography.

The in vitro stability of  $^{76}\text{Br}$ -L19-SIP in mouse serum at 37°C was investigated by radio-FPLC analysis. A sample with 91% RCP was used for this experiment. In 48 h, no

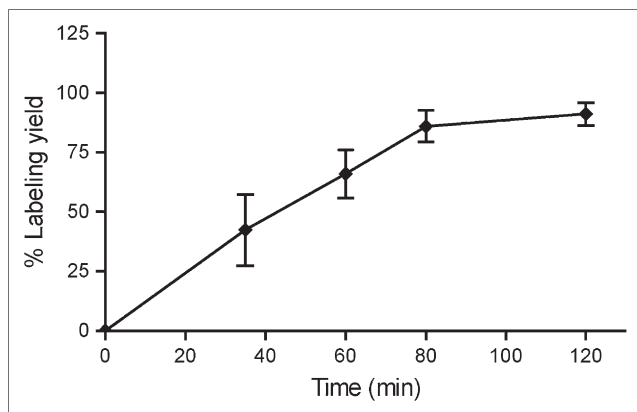


**FIGURE 1.** Effect of reaction time on labeling yield of BPO-catalyzed L19-SIP  $^{76}\text{Br}$ -bromination at 0°C ( $< 37$  MBq  $^{76}\text{Br}$  used in the reactions;  $n = 3$ ). Data are expressed as mean  $\pm$  SD.

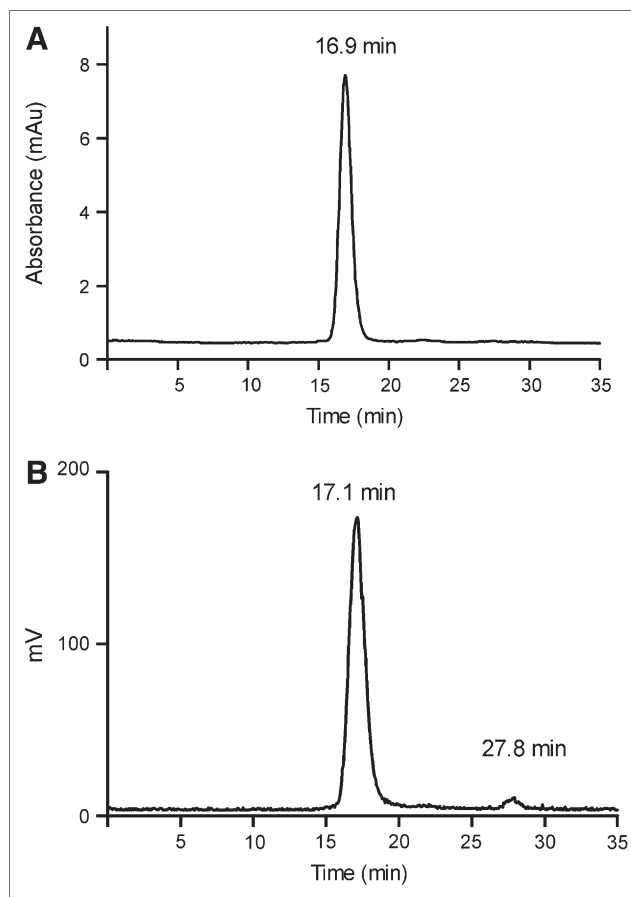


**FIGURE 2.** Representative FPLC chromatograms of L19-SIP (A) and NAP-5-purified  $^{76}\text{Br}$ -L19-SIP ( $^{76}\text{Br}$ -L19-SIP) (B): Retention time [ $R_t$ ] = 16.9–17.1 min;  $^{76}\text{Br}$ -bromide:  $R_t = 27.8$  min). mAu = milliabsorbance units.

additional  $^{76}\text{Br}$ -bromide was detected on the radiochromatogram (Fig. 3A). However, the formation of high-molecular-weight impurities was observed (21% of total activity in 48 h; Fig. 3C). In a similar experiment, the formation of high-molecular-weight impurities was observed also when incubating  $^{125}\text{I}$ -L19-SIP in mouse serum, but to a lesser extent compared with the  $^{76}\text{Br}$ -labeled analog (up to 7% of total activity in 48 h, Fig. 3B). Similarly, no radiolabel release from  $^{125}\text{I}$ -L19-SIP was observed in vitro.

### Biodistribution Studies

F9 tumor-bearing mice were injected with a low dose of  $^{76}\text{Br}$ -L19-SIP ( $\sim 1.3$  MBq/mouse corresponding to  $\sim 0.35$  mg antibody per kg mouse weight). The obtained biodistribution data (Table 1) showed a high and persistent activity accumulation in the F9 tumors ( $18.1 \pm 7.6$ ,  $9.3 \pm 3.5$ , and  $14.3 \pm 1.6$  %ID/g at 5, 24, and 48 h, respectively) and in other ED-B fibronectin-expressing organs (ovaries and uterus). A significant amount of radioactivity was also observed in blood ( $22.4 \pm 3.7$ ,  $7.6 \pm 1.8$ , and  $8.1 \pm 1.7$  %ID/g at 5, 24, and 48 h after injection, respectively), in blood-rich organs (such as lung and heart, which were not perfused before counting), and in other

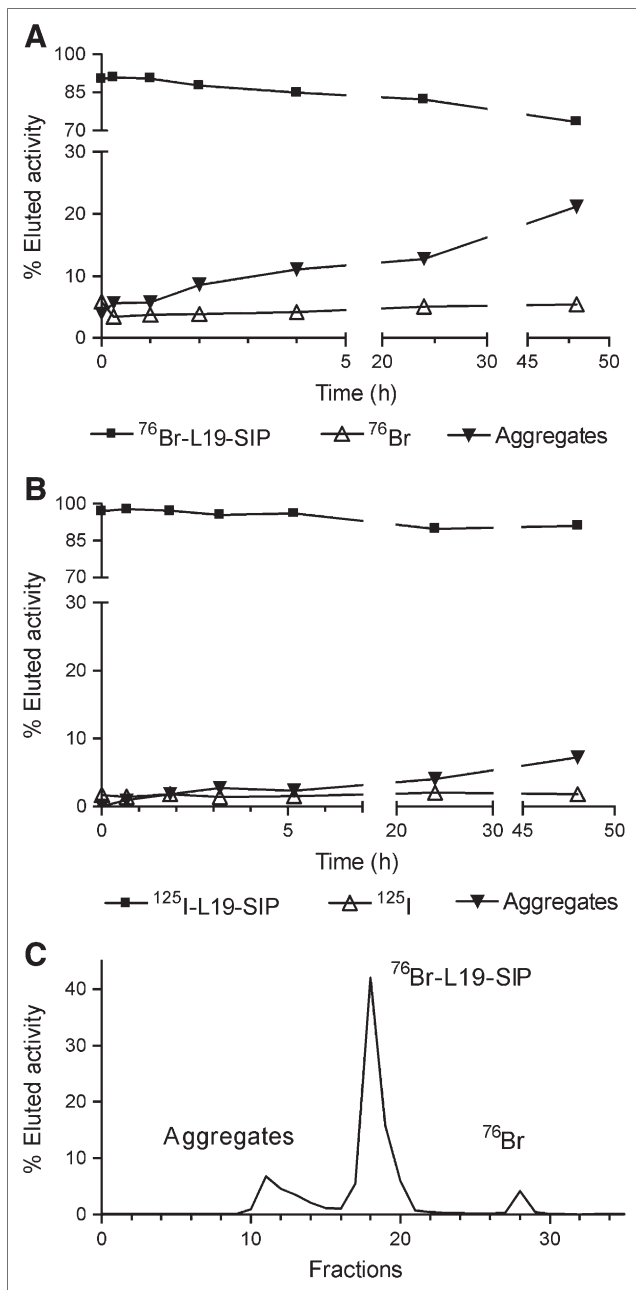


**FIGURE 3.** In vitro stability of <sup>76</sup>Br-L19-SIP (A) and <sup>125</sup>I-L19-SIP (B) and radiochromatogram of <sup>76</sup>Br-L19-SIP after 48-h incubation in mouse serum at 37°C (C).

nontarget organs. Slow clearance was observed in many of the nontarget organs (except for muscle and bone) up to 48 h after injection as a consequence of slow radioactivity elimination through the urinary tract ( $4.7 \pm 0.9$  %ID at 48 h after injection in urine).

### Imaging Studies

Four tumor-bearing mice were injected with a higher dose of <sup>76</sup>Br-L19-SIP (~13 MBq/mouse corresponding to ~1.4 mg antibody per kg mouse weight). microPET images were collected at 5, 24, and 48 h after injection and

**TABLE 1**  
Biodistribution of <sup>76</sup>Br-L19-SIP in F9 Tumor-Bearing 129/sv Mice at Various Time Points

	Postinjection biodistribution time (h)		
	5	24	48
<b>Uptake (%ID/g)</b>			
Blood	22.4 ± 3.7	7.6 ± 1.8	8.1 ± 1.7
Lung	11.4 ± 2.0	5.3 ± 0.9	5.8 ± 0.9
Liver	5.0 ± 0.3	2.3 ± 0.6	2.5 ± 0.5
Spleen	5.7 ± 0.6	3.4 ± 0.5	2.9 ± 0.7
Kidney	9.4 ± 1.9	4.3 ± 1.0	4.1 ± 1.2
Muscle	2.5 ± 0.2	4.0 ± 1.1	2.6 ± 0.0
Fat	1.7 ± 0.5	1.4 ± 0.5	0.9 ± 0.2
Heart	6.2 ± 0.6	2.4 ± 0.5	2.7 ± 0.5
Bone	3.6 ± 0.6	5.6 ± 1.6	2.6 ± 0.4
Uterus	13.5 ± 6.3	9.6 ± 3.0	6.0 ± 1.0
Ovaries	7.0 ± 2.3	2.7 ± 1.2	1.8 ± 0.3
Thyroid	5.5 ± 2.5	3.5 ± 1.6	2.4 ± 0.3
Tumor	18.1 ± 7.6*	9.3 ± 3.5*	14.3 ± 1.6
<b>Tumor/tissue ratio</b>			
Tumor/blood	0.8 ± 0.4	1.2 ± 0.5	1.8 ± 0.4
Tumor/lung	1.6 ± 0.7	1.8 ± 0.7	2.5 ± 0.5
Tumor/liver	3.6 ± 1.5	4.1 ± 1.9	5.8 ± 1.3
Tumor/spleen	3.2 ± 1.4	2.7 ± 1.1	4.9 ± 1.3
Tumor/kidney	1.9 ± 0.9	2.2 ± 1.0	3.4 ± 1.1
Tumor/muscle	7.3 ± 3.1	2.3 ± 1.1	5.6 ± 0.6
Tumor/fat	10.5 ± 5.4	6.7 ± 3.6	15.1 ± 3.6
Tumor/heart	2.9 ± 1.3	3.9 ± 1.7	5.3 ± 1.1
Tumor/bone	5.0 ± 2.3	1.7 ± 0.8	5.5 ± 1.0
Tumor/uterus	1.3 ± 0.8	1.0 ± 0.5	2.4 ± 0.5
Tumor/ovaries	2.6 ± 1.4	3.5 ± 2.0	7.9 ± 1.4
Tumor/thyroid	3.3 ± 2.0	2.7 ± 1.6	5.9 ± 0.9
<b>Excretion (%ID)</b>			
Urine	0.12 ± 0.04	1.5 ± 1.3	4.7 ± 0.9
Feces	—	—	0.18 ± 0.04

\**P* = 0.093.

Data are presented as %ID/g ± SD (*n* = 3 or 4).

coregistered with microCT at the last 2 time points. Specific accumulation of radioactivity in the ED-B fibronectin-expressing tumors was clearly visible at each considered time point (Figs. 4 and 5). As predicted from the biodistribution studies, the microPET images acquired at 5 h after injection exhibited a high background activity, mainly in the abdominal area. The heart and the aorta of the mice were clearly delineated at 5 h after injection due to the high amount of radioactivity in the blood (Figs. 4A and 4D). At this early time point, also the kidneys were visible. At 24 h after injection, the background activity was visibly lower compared with the earlier time point (Figs. 4B and 4E), whereas the stomach of both mice became detectable. At 48 h after injection, some background activity was still present and the most visible organs were the tumors, stomachs, and bladders (Figs. 4C and 4F). Semiquantitative analysis of microPET images (Table 2) confirmed the results of the biodistribution experiment. The tumor SUV was high and persistent at each considered time point ( $2.4 \pm 0.5$  at 5 h,  $2.7 \pm 0.1$  at 24 h, and  $2.4 \pm 0.2$  at 48 h after injection) and

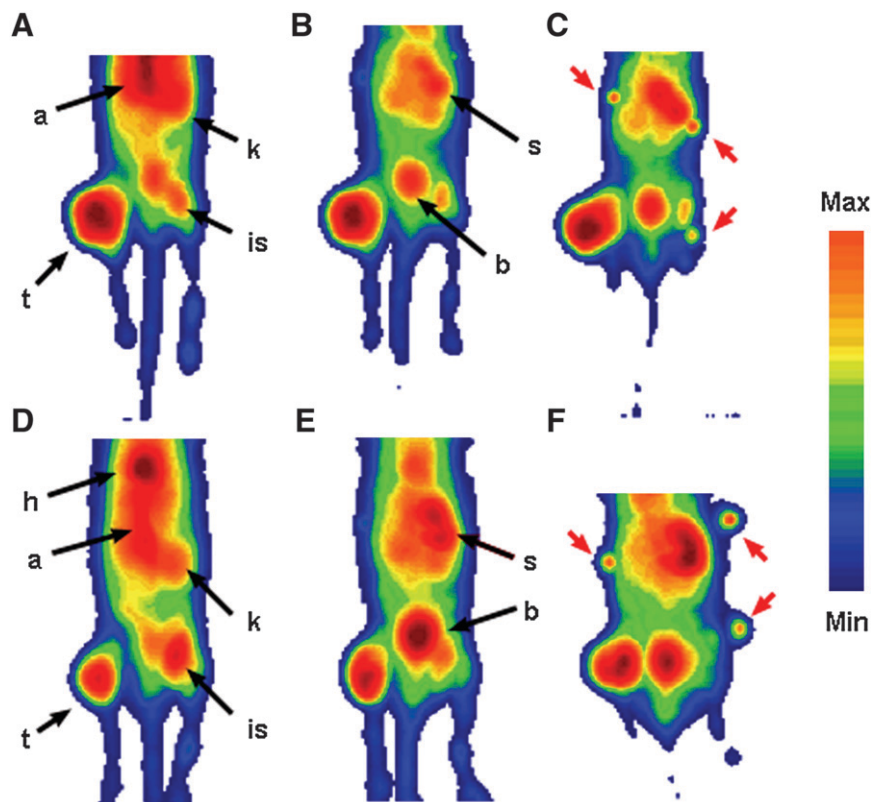


**FIGURE 4.** Coronal microPET projection images of 2 F9 tumor-bearing mice at 5 h (A and D), 24 h (B and E), and 48 h (C and F) after injection. Imaging intensity was decay-corrected and scaled by maximal/minimal (Max/Min) frame. a = aorta; t = tumor; h = heart; k = kidney; is = injection site; s = stomach; b = bladder. Red arrows indicate the fiducial markers used for microPET/microCT co-registration.

approximately 4- to 5-fold higher compared with that of the muscle. The stomach showed no specific accumulation of radioactivity over the surrounding tissues at 5 h after injection but became visible at later time points (SUV:  $1.9 \pm 0.0$  at both 24 and 48 h after injection).

#### Metabolism Studies

Normal mice were used for this study ( $n = 3$  per time point). The animals were injected with  $\sim 0.2$  mg of  $^{76}\text{Br}$ -L19-SIP per kg body weight ( $\sim 1.8$  MBq/mouse; RCP > 95%; 84% immunoreactivity). Serum and urine samples were collected and analyzed by radio-FPLC at selected time points. In serum, the amount of residual intact antibody was  $86.1\% \pm 1.7\%$  at 2 h after injection,  $73.5\% \pm 0.5\%$  at 5 h after injection, and  $24.7\% \pm 0.9\%$  at 24 h after injection (Fig. 6A) and the residual immunoreactivity of  $^{76}\text{Br}$ -L19-SIP was 65%, 66%, and 21% as determined by affinity chromatography. Small amounts of intact antibody were also detected in urine (Fig. 6B;  $7.7\% \pm 0.1\%$ ,  $5.8\% \pm 0.6\%$ , and  $0.8\% \pm 0.3\%$  of total eluted activity at 2, 5, and 24 h after injection, respectively). However, the majority of the excreted activity was due to  $^{76}\text{Br}$ -bromide.

#### DISCUSSION

Molecular imaging of tumor neovasculature is an important feature for and early assessment of response to anti-angiogenic cancer therapy. To date, the application of PET to angiogenesis imaging has been explored mostly by using radiolabeled RGD peptides targeting  $\alpha_v\beta_3$  integrins. Small

monomeric and dimeric RGD derivatives labeled with  $^{64}\text{Cu}$  (11) and  $^{18}\text{F}$  (8,12,14) showed a moderate accumulation in solid tumors but washed out within few hours after tracer administration. A higher and more persistent uptake was observed with a tetrameric RGD peptide, reasonably due to

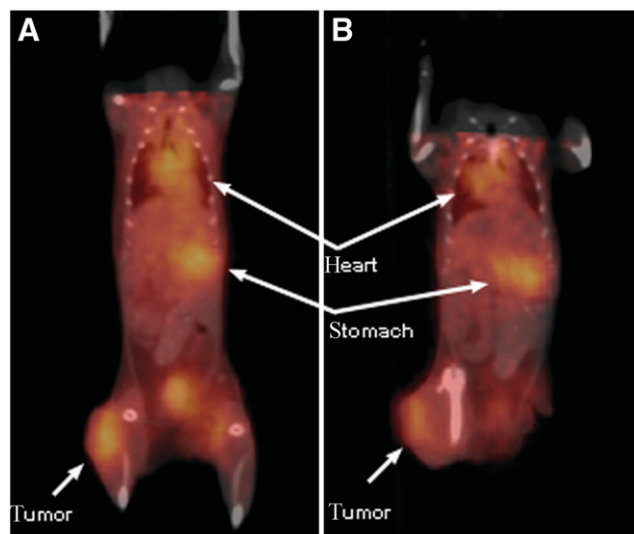


**FIGURE 5.** Coregistered microPET and microCT coronal images of one F9 tumor-bearing mouse injected with  $^{76}\text{Br}$ -L19-SIP at 24 h (A) and 48 h (B) after injection. In B, animal was slightly offset from full supine position because of tumor in right hindlimb. Imaging intensity was decay-corrected and scaled by maximal/minimal frame.

**TABLE 2**

Comparative Organ-by-Organ SUVs for  $^{76}\text{Br}$ -L19-SIP from Quantitation of microPET Images in F9 Tumor-Bearing Mice ( $n = 4$ )

SUV	Postinjection imaging time (h)		
	5	24	48
Tumor	2.4 ± 0.5	2.7 ± 0.1	2.4 ± 0.2
Muscle*	0.6 ± 0.2	0.6 ± 0.0	0.5 ± 0.0
Stomach	ND <sup>†</sup>	1.9 ± 0.0	1.9 ± 0.0

\*Lumbar muscle.

<sup>†</sup>Organ could not be detected on microPET images at this time point.

Data were obtained from averaging 3D ROIs in selected organs and are presented as mean SUV ± SD.

polyvalency and size (13). In all of these studies, however, variable tracer amounts were retained in nontarget organs such as lung, liver, kidney, and intestine. Despite this, a good correlation between  $\alpha_v\beta_3$  expression and tumor uptake was observed in humans (10), and a variety of cancers was successfully imaged in a small clinical trial (9). High and prolonged uptake in angiogenic tumor vessels was obtained also by using small proteins such as the  $^{64}\text{Cu}$ -labeled VEGF121 (5) and the  $^{124}\text{I}$ -labeled VG76e (7), targeting the VEGFR. Consequently, a radioiodinated humanized derivative of VEGF121 was tested as an antivascular therapeutic agent in a phase I clinical trial (6). Nonetheless, these compounds also showed nonspecific accumulation in nontarget organs such as liver, kidney, and lung.

The oncofetal domain (ED-B) of fibronectin has proven to be another powerful target on solid tumor neovasculature (15–17,34,35), and an antibody with subnanomolar affinity for ED-B fibronectin (L19) has been produced (18). Recently, radioimmunotherapy and SPECT with L19 derivatives labeled with various radionuclides ( $^{131}\text{I}$ ,  $^{123}\text{I}$ ,  $^{99\text{m}}\text{Tc}$ ) gave very promising results in different tumor models (20–24) and in a small clinical trial (19). For these reasons, we decided to explore targeting of ED-B fibronectin with a positron emitter–labeled L19-SIP for PET of tumor neovasculature.

Toward this aim, we have chosen  $^{76}\text{Br}$ , a radiohalogen decaying 55% by positron-emission (maximum  $\beta$ -energy,  $[\beta_{\text{max}}] = 3.941 \text{ MeV}$ ). Despite the emission of prompt  $\gamma$ -rays in the energy window of PET scanners (559 and 657 keV), imaging with  $^{76}\text{Br}$  is feasible (29,36), and the favorable half-life ( $t_{1/2} = 16.2 \text{ h}$ ) makes this radionuclide a good candidate for imaging antibodies in vivo (27–31). The radiobromination of L19-SIP was performed by means of an enzymatic method using BPO (28,37). This direct halogenation approach was chosen because of it is straightforward and because the BPO/ $\text{H}_2\text{O}_2$  mixture was proven to be fast and effective in producing radiobrominated antibodies with retained immunoreactivity (27–29). In fact, L19-SIP was labeled at a low dose of  $^{76}\text{Br}$  (<37 MBq) in high yield and in a short time (Fig. 1).

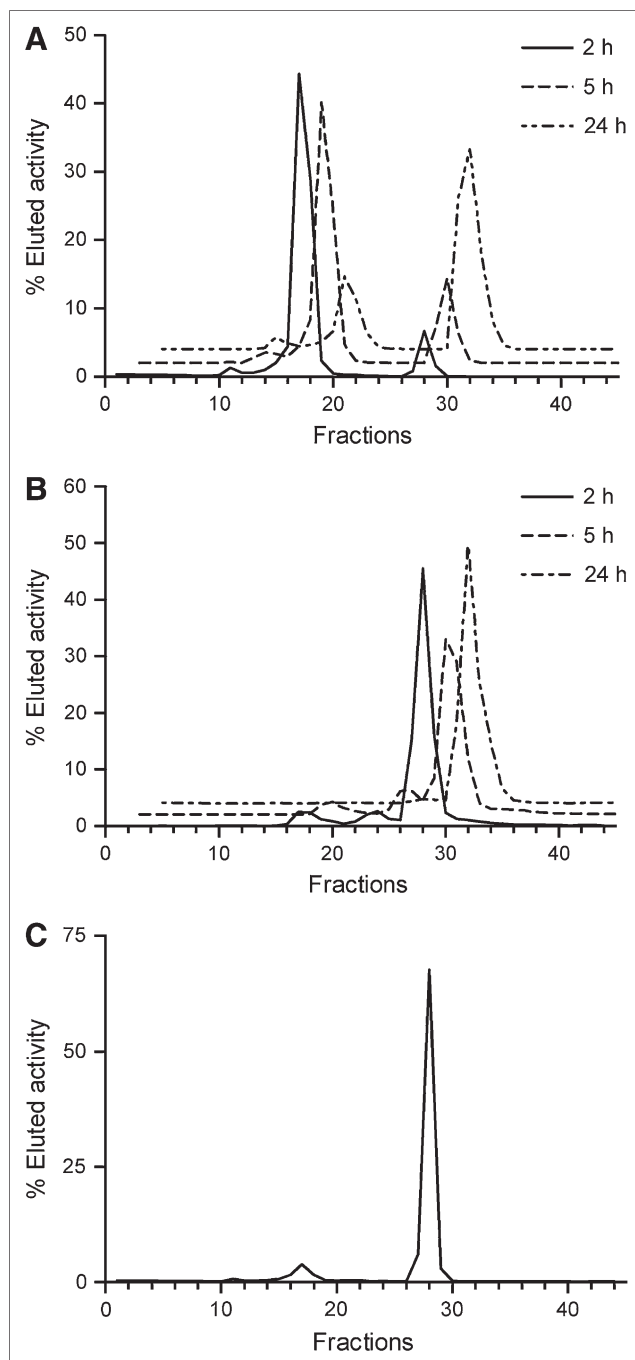


**FIGURE 6.** In vivo metabolism: radiochromatograms of plasma (A) and urine (B) of normal mice injected with  $^{76}\text{Br}$ -L19-SIP and radiochromatogram of plasma (C) withdrawn from a F9 tumor-bearing mouse microPET imaging (48 h after injection).

When using  $>37 \text{ MBq } ^{76}\text{Br}$ , however, no significant antibody labeling was observed. Instead, the presence of low-molecular-weight radioactive impurities in the reaction mixture was detected by radio-FPLC (data not shown), possibly as a consequence of radiolysis. To avoid this, an optimized protocol could be established by removing any solvent right after the target process. NAP-5 purification of the labeling

mixture proved to be a suitable way for a timely and cost-effective separation of the product. The values of immunoreactivity obtained for  $^{76}\text{Br}$ -L19-SIP were slightly lower compared with those reported for  $^{125/131}\text{I}$ -labeled analogs (20,24). This was reasonably due to the presence of residual  $^{76}\text{Br}$ -bromide in the NAP-5-purified antibody sample (Fig. 2B). Even though the radiobrominated antibody was found to be stable over 48 h in vitro (Fig. 3A), the formation of some high-molecular-weight by-products occurred over time (Fig. 3C), suggesting the formation of aggregates. A similar behavior was observed for  $^{125}\text{I}$ -L19-SIP (Fig. 3B).

The tumor model used to evaluate  $^{76}\text{Br}$ -L19-SIP as an angiogenesis-targeting agent is a fast-growing murine teratocarcinoma (F9) expressing high levels of ED-B fibronectin (20,24,25). Our biodistribution data showed elevated and fast accumulation of  $^{76}\text{Br}$ -L19-SIP in F9 tumors (Table 1), similar to that of  $^{125}\text{I}$ - and  $^{111}\text{In}$ -labeled analogs (20,25) and higher than that of a smaller antibody fragment labeled with  $^{99\text{m}}\text{Tc}$  (24) in the same tumor model. Furthermore, the tracer accumulation in the tumor was comparable to that reported for VEGFR targeting PET tracers (5,7) and higher than that observed with  $\alpha_3\beta_3$  targeting peptides (8,11–14) in a variety of tumor models.

Specific targeting of ED-B fibronectin was confirmed also by the high  $^{76}\text{Br}$ -L19-SIP uptake in the mouse reproductive organs (uterus and ovaries), which physiologically express the ED-B of fibronectin (15,34). Unfortunately, long retention of radioactivity in blood and very slow renal excretion were also observed. As a consequence, the background activity in nontarget organs was higher than that reported for the  $^{125}\text{I}$ -labeled L19-SIP, and this resulted in lower target-to-nontarget ratios in all of the considered organs but thyroid (Table 1). Despite the slow blood kinetics and the high activity in nontarget organs, such as muscle and bone, high imaging contrast was achieved and the F9 tumors implanted in the hindlimb were clearly imaged by microPET at each considered time point (Figs. 4 and 5). The SUV data obtained from the semiquantitative analysis of microPET images (Table 2) confirmed high and persistent  $^{76}\text{Br}$ -L19-SIP uptake in the tumor, which was 4- to 5-fold higher compared with that in nontarget tissue (lumbar muscle) at each considered time point.

The presence of activity in nontarget organs and the persistent activity in blood suggest partial debromination of  $^{76}\text{Br}$ -L19-SIP in vivo. In fact, when mice were administered radiobromide, high radioactivity levels were still detected in blood after 48 h (28,38). Furthermore, autoradiographic studies in mice reported high radioactivity concentration in the gastric mucosa as early as 5 min after injection of  $^{82}\text{Br}$ -bromide (39). In our experiments, the slow activity accumulation in the stomach, which appeared on the microPET images only 24 h after injection (Fig. 4; Table 2), indicates that some debromination of  $^{76}\text{Br}$ -L19-SIP occurred within several hours of the tracer administration. The results of a metabolism study in normal mice confirmed slow in vivo debromination of  $^{76}\text{Br}$ -L19-SIP. In fact, low amounts of

$^{76}\text{Br}$ -bromide were detected in serum at 2 and 5 h after injection, whereas, at 24 h after injection, most of the activity eluted from the FPLC column was free  $^{76}\text{Br}$  (Fig. 6A). At the end of the microPET/microCT sessions, we performed the same test on the plasma of the mice used for imaging. At this time point,  $2.2\% \pm 0.2\%$  ( $n = 2$ ) of the administered radioactivity was still present in blood but only a small fraction of this was due to intact antibody, whereas most of the radioactivity was free bromide (Fig. 6C). Partial in vivo dehalogenation was observed also for  $^{125}\text{I}$ -L19-SIP. In fact, the reported radioactivity uptake values in the stomach (23) and nonblocked thyroid (20,22) are comparable to those obtained when administering the mice free radioiodide (28,40). Low background uptake in nontarget organs was observed for  $^{125}\text{I}$ -L19-SIP (20,22,25), reasonably because free iodide clears rapidly from the blood and is taken up by the thyroid or is excreted through the kidneys (28,40).

Therefore, to improve the in vivo performances of the radiobrominated antibody, indirect labeling strategies that may lead to less metabolism or radiocatabolites with short in vivo half lives (26,30,31) will have to be considered.

## CONCLUSION

In this study, we investigated the possible use of a  $^{76}\text{Br}$ -labeled L19 derivative to image the neovasculature of tumors undergoing angiogenesis with PET. Although the directly labeled antibody underwent partial in vivo dehalogenation, with consequent high-activity background and slow clearance, the targeting properties of  $^{76}\text{Br}$ -L19-SIP for ED-B fibronectin were confirmed. In fact, the F9 tumors exhibited a high and persistent radiotracer uptake and were clearly visualized by microPET at each considered time point. Further studies are needed to optimize the in vivo performances of  $^{76}\text{Br}$ -L19-SIP. However, this is an important step toward the imaging of angiogenesis biomarkers with PET.

## ACKNOWLEDGMENTS

The authors thank Richard Laforest, Nicole Fettig, Margaret Morris, Dawn Werner, Lori Strong, Jerrel Rutlin, Susan Adams, and Terry Sharp for excellent assistance in the biodistribution and imaging studies as well as Dieter Moosmayer and Guido Malawski for production and purification of the L19-SIP antibody fragment and Lucie Tang, Douglas J. Rowland, and Rajendra Singh for  $^{76}\text{Br}$  production. The production of  $^{76}\text{Br}$  at Washington University School of Medicine is supported by NCI grant R24 CA86307.

## REFERENCES

1. Folkman J. Angiogenesis in cancer, vascular, rheumatoid and other disease. *Nat Med.* 1995;1:27–30.
2. Eskens F. Angiogenesis inhibitors in clinical development: Where are we now and where are we going? *Br J Cancer.* 2004;90:1–7.

3. Kurdziel KA, Bacharach SL, Carrasquillo JA, et al. Using PET  $^{18}\text{F}$ -FDG,  $^{11}\text{C}$ O, and  $^{15}\text{O}$ -water for monitoring prostate cancer during a phase II anti-angiogenic drug trial with thalidomide. *Clin Positron Imaging*. 2000;3:144.
4. Kracht LW, Friese M, Herholz K, et al. Methyl- $^{11}\text{C}$ -L-methionine uptake as measured by positron emission tomography correlates to microvessel density in patients with glioma. *Eur J Nucl Med Mol Imaging*. 2003;30:868–873.
5. Cai W, Chen K, Mohamedali KA, et al. PET of vascular endothelial growth factor receptor expression. *J Nucl Med*. 2006;47:2048–2056.
6. Jayson GC, Zweit J, Jackson A, et al. Molecular imaging and biological evaluation of HuMV833 anti-VEGF antibody: implications for trial design of antiangiogenic antibodies. *J Natl Cancer Inst*. 2002;94:1484–1493.
7. Collingridge DR, Carroll VA, Glaser M, et al. The development of  $^{124}\text{I}$ iodinated-VG76e: a novel tracer for imaging vascular endothelial growth factor in vivo using positron emission tomography. *Cancer Res*. 2002;62:5912–5919.
8. Haubner R, Wester H-J, Weber WA, et al. Noninvasive imaging of  $\alpha_v\beta_3$  integrin expression using  $^{18}\text{F}$ -labeled RGD-containing glycopeptide and positron emission tomography. *Cancer Res*. 2001;61:1781–1785.
9. Beer AJ, Haubner R, Goebel M, et al. Biodistribution and pharmacokinetics of the  $\alpha_v\beta_3$ -selective tracer  $^{18}\text{F}$ -galacto-RGD in cancer patients. *J Nucl Med*. 2005;46:1333–1341.
10. Beer AJ, Haubner R, Sarbia M, et al. Positron emission tomography using  $^{18}\text{F}$ galacto-RGD identifies the level of integrin  $\alpha_v\beta_3$  expression in man. *Clin Cancer Res*. 2006;12:3942–3949.
11. Chen X, Hou Y, Tohme M, et al. Pegylated Arg-Gly-Asp peptide:  $^{64}\text{Cu}$  labeling and PET imaging of brain tumor  $\alpha_v\beta_3$ -integrin expression. *J Nucl Med*. 2004;45:1776–1783.
12. Cai W, Zhang X, Wu Y, Chen XA. Thiol-reactive  $^{18}\text{F}$ -labeling agent, N-[2-(4- $^{18}\text{F}$ -fluorobenzamido)ethyl]maleimide, and synthesis of RGD peptide-based tracer for PET imaging of  $\alpha_v\beta_3$  integrin expression. *J Nucl Med*. 2006;47:1172–1180.
13. Wu Y, Zhang X, Xiong Z, et al. microPET imaging of glioma integrin  $\alpha_v\beta_3$  expression using  $^{64}\text{Cu}$ -labeled tetrameric RGD peptide. *J Nucl Med*. 2005;46:1707–1718.
14. Zhang X, Xiong Z, Wu Y, et al. Quantitative PET imaging of tumor integrin  $\alpha_v\beta_3$  expression with  $^{18}\text{F}$ -FRGD2. *J Nucl Med*. 2006;47:113–121.
15. Castellani P, Viale G, Dorcaratto A, et al. The fibronectin isoform containing the ED-B oncofetal domain: a marker of angiogenesis. *Int J Cancer*. 1994;59:612–618.
16. Menrad A, Menssen HD. ED-B fibronectin as a target for antibody-based cancer treatments. *Expert Opin Ther Targets*. 2005;9:491–500.
17. Birchler MT, Milisavljevic D, Pfaltz M, et al. Expression of the extradomain B of fibronectin, a marker of angiogenesis, in head and neck tumors. *Laryngoscope*. 2003;113:1231–1237.
18. Pini A, Viti F, Santucci A, et al. Design and use of a phage display library. human antibodies with subnanomolar affinity against a marker of angiogenesis eluted from a two-dimensional gel. *J Biol Chem*. 1998;273:21769–21776.
19. Santimaria M, Moscatelli G, Viale GL, et al. Immunoscintigraphic detection of the ED-B domain of fibronectin, a marker of angiogenesis, in patients with cancer. *Clin Cancer Res*. 2003;9:571–579.
20. Berndorff D, Borkowski S, Sieger S, et al. Radioimmunotherapy of solid tumors by targeting extra domain B fibronectin: identification of the best-suited radioimmunoconjugate. *Clin Cancer Res*. 2005;11(19 pt 2):7053s–7063s.
21. Spaeth N, Wyss MT, Pahnke J, et al. Radioimmunotherapy targeting the extra domain B of fibronectin in C6 rat gliomas: a preliminary study about the therapeutic efficacy of iodine-131-labeled SIP(L19). *Nucl Med Biol*. 2006;33:661–666.
22. Moosmayer D, Berndorff D, Chang C-H, et al. Bispecific antibody pretargeting of tumor neovasculature for improved systemic radiotherapy of solid tumors. *Clin Cancer Res*. 2006;12:5587–5595.
23. Tijink BM, Neri D, Leemans CR, et al. Radioimmunotherapy of head and neck cancer xenografts using  $^{131}\text{I}$ -labeled antibody L19-SIP for selective targeting of tumor vasculature. *J Nucl Med*. 2006;47:1127–1135.
24. Berndorff D, Borkowski S, Moosmayer D, et al. Imaging of tumor angiogenesis using  $^{99\text{m}}\text{Tc}$ -labeled human recombinant anti-ED-B fibronectin antibody fragments. *J Nucl Med*. 2006;47:1707–1716.
25. Borsi L, Balza E, Bestagno M, et al. Selective targeting of tumoral vasculature: comparison of different formats of an antibody (L19) to the ED-B domain of fibronectin. *Int J Cancer*. 2002;102:75–85.
26. Hoglund J, Tolmachev V, Orlova A, Lundqvist H, Sundin A. Optimized indirect  $^{76}\text{Br}$ -bromination of antibodies using n-succinimidyl para- $^{76}\text{Br}$ bromobenzoate for radioimmuno PET. *Nucl Med Biol*. 2000;27:837–843.
27. Lovqvist A, Sundin A, Ahlstrom H, Carlsson J, Lundqvist H.  $^{76}\text{Br}$ -Labeled monoclonal anti-CEA antibodies for radioimmuno positron emission tomography. *Nucl Med Biol*. 1995;22:125–131.
28. Lovqvist A, Sundin A, Ahlstrom H, Carlsson J, Lundqvist H. Pharmacokinetics and experimental PET imaging of a bromine-76-labeled monoclonal anti-CEA antibody. *J Nucl Med*. 1997;38:395–401.
29. Lovqvist A, Sundin A, Roberto A, Ahlstrom H, Carlsson J, Lundqvist H. Comparative PET imaging of experimental tumors with bromine-76-labeled antibodies, fluorine-18-fluorodeoxyglucose and carbon-11-methionine. *J Nucl Med*. 1997;38:1029–1035.
30. Mume E, Orlova A, Malmstrom P-U, Lundqvist H, Sjoberg S, Tolmachev V. Radiobromination of humanized anti-HER2 monoclonal antibody trastuzumab using N-succinimidyl 5-bromo-3-pyridinecarboxylate, a potential label for immunoPET. *Nucl Med Biol*. 2005;32:613–622.
31. Winberg KJ, Persson M, Malmstrom P-U, Sjoberg S, Tolmachev V. Radiobromination of anti-HER2/neu/ErbB-2 monoclonal antibody using the p-isothiocyanatobenzene derivative of the  $^{76}\text{Br}$ undecahydro-bromo-7,8-dicarba-nido-undecaborate(1-) ion. *Nucl Med Biol*. 2004;31:425–433.
32. Glaser M, Luthra SK, Brady F. Applications of positron-emitting halogens in PET oncology (review). *Int J Oncol*. 2003;22:253–267.
33. Tolmachev V, Lovqvist A, Einarsson L, Schultz J, Lundqvist H. Production of  $^{76}\text{Br}$  by a low-energy cyclotron. *Appl Radiat Isot*. 1998;49:1537–1540.
34. Carnemolla B, Balza E, Siri A, et al. A tumor-associated fibronectin isoform generated by alternative splicing of messenger RNA precursors. *J Cell Biol*. 1989;108:1139–1148.
35. Ruoslahti E. Fibronectin and its integrin receptors in cancer. *Adv Cancer Res*. 1999;76:1–20.
36. Beattie BJ, Finn RD, Rowland DJ, Pentlow KS. Quantitative imaging of bromine-76 and yttrium-86 with PET: a method for the removal of spurious activity induced by cascade gamma rays. *Med Phys*. 2003;30:2410–2423.
37. McElvany KD, Welch MJ. Characterization of bromine-77-labeled proteins prepared by using bromoperoxidase. *J Nucl Med*. 1980;21:953–960.
38. Lee H, Finck BN, Jones LA, Welch MJ, Mach RH. Synthesis and evaluation of a bromine-76-labeled PPAR $\gamma$  antagonist 2-bromo-5-nitro-N-phenylbenzamide. *Nucl Med Biol*. 2006;33:847–854.
39. Soremark R, Ullberg S. Distribution of bromine in mice: an autoradiographic study with Br-82. *Int J Appl Radiat Isot*. 1960;8:192–197.
40. Zuckier LS, Dohan O, Li Y, Chang CJ, Carrasco N, Dadachova E. Kinetics of perhenate uptake and comparative biodistribution of perhenate, pertechnetate, and iodide by NaI symporter-expressing tissues in vivo. *J Nucl Med*. 2004;45:500–507.